

# Electronic supplementary information (ESI): Strong size selectivity in the self-assembly of rounded nanocubes into 3D mesocrystals

Elisabeth Josten,<sup>\*,†,#</sup> Manuel Angst,<sup>†</sup> Artur Glavic,<sup>‡</sup> Paul Zakalek,<sup>†</sup>  
Ulrich Rücker,<sup>†</sup> Oliver H. Seeck,<sup>¶</sup> András Kovács,<sup>§</sup> Erik Wetterskog,<sup>||</sup> Emmanuel  
Kentzinger,<sup>†</sup> Rafal E. Dunin-Borkowski,<sup>§</sup> Lennart Bergström,<sup>⊥</sup> and  
Thomas Brückel<sup>†</sup>

<sup>†</sup>*Jülich Centre for Neutron Science (JCNS) and Peter Grünberg Institute (PGI),  
JARA-FIT, Forschungszentrum Jülich GmbH, 52425 Jülich, Germany*

<sup>‡</sup>*Laboratory for Neutron Scattering and Imaging, Paul Scherrer Institut, 5232 Villigen PSI,  
Switzerland*

<sup>¶</sup>*Deutsches Elektronen-Synchrotron DESY, Notkestraße 85, 22607 Hamburg, Germany*

<sup>§</sup>*Ernst Ruska-Centre for Microscopy and Spectroscopy with Electrons (ER-C) and  
Peter Grünberg Institute (PGI), Forschungszentrum Jülich, 52425 Jülich, Germany*

<sup>||</sup>*Department of Engineering Sciences, Ångström Laboratory, Uppsala University, 751 21  
Uppsala, Sweden*

<sup>⊥</sup>*Department of Materials and Environmental Chemistry, Stockholm University, 10691  
Stockholm, Sweden*

<sup>#</sup>*Current address: Ernst Ruska-Centre for Microscopy and Spectroscopy with Electrons  
and Peter Grünberg Institute, Forschungszentrum Jülich, 52425 Jülich, Germany*

E-mail: e.josten@fz-juelich.de

# S1. SAXS analysis and rounded cubical form factor

## S1.1 Small angle x-ray scattering (SAXS)

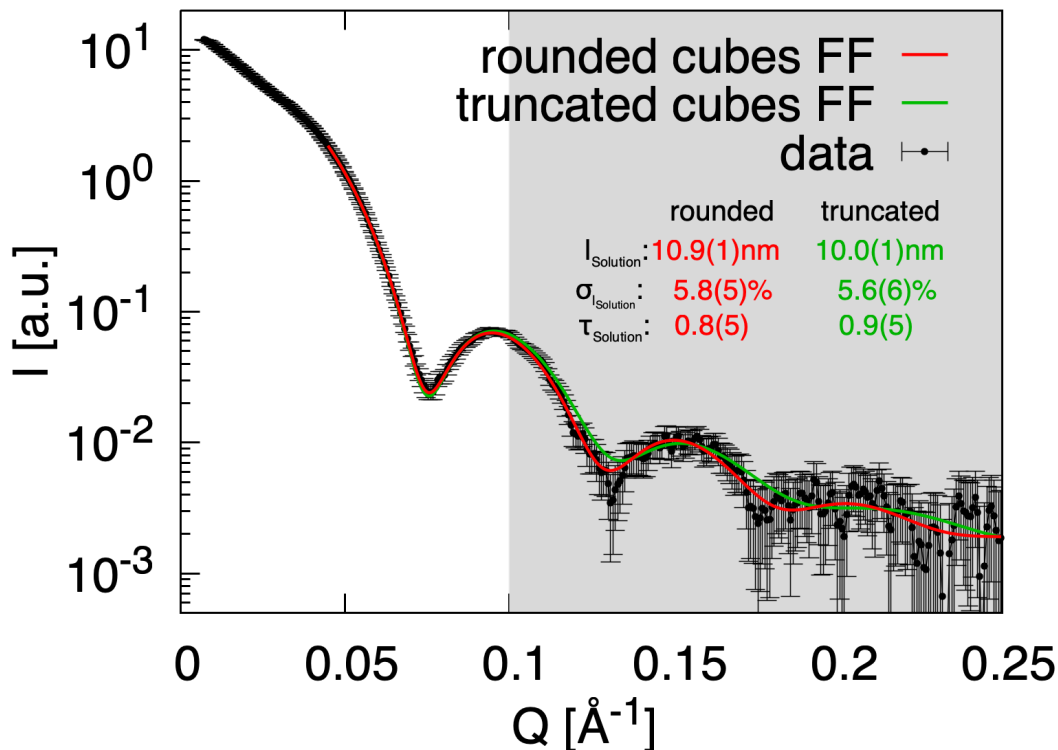


Figure S1: SAXS characterization of “cube-like” nanoparticles. The experimental data (circles with error bars) are fitted with a truncated cube (green line) and with a rounded cube (red line) model. The optimal fit parameters for both models are given in the figure.

The particle shapes of the nanoparticles were determined from the analysis of SAXS data (which is only sensitive to the shape of the inorganic core).

For the “cube-like” nanoparticles, a Bruker AXS Nanostar SAXS instrument (Cu  $K\alpha$ ) was used, with the nanoparticles in a dilute solution ( $0.1 \times 10^{14}$  NP/ml in Toluol) in Hilgenberg borosilicate glass capillaries. The measured data, time-normalized and corrected for detector sensitivity, empty cell, and dark current, and radially averaged, is shown in Fig. S1 (circles with error bars). A minor contribution by a structure factor is negligible except possibly at very small  $Q$ .

The data in the  $Q$  region from  $0.05 - 0.25 \text{ \AA}^{-1}$  were fitted with two models: the (flat) truncated cube model used earlier<sup>1</sup> on nanoparticles grown in the same way (green line) and a new model with rounded cubes, described in Sec. S1.2 (red line). Both models include a log-normal size distribution and provide a reasonable description of the data (the best fit parameters are given in the figure; note that the fitted size distribution is very similar for the two models), but particularly in the high- $Q$  region (shaded in grey in Fig. S1) there are

significant deviations, with the rounded cube model better fitting the experimental data. Therefore, the rounded cube model is used in this paper for the “cube-like” nanoparticles.

## S1.2 Model: Rounded cubical form factor

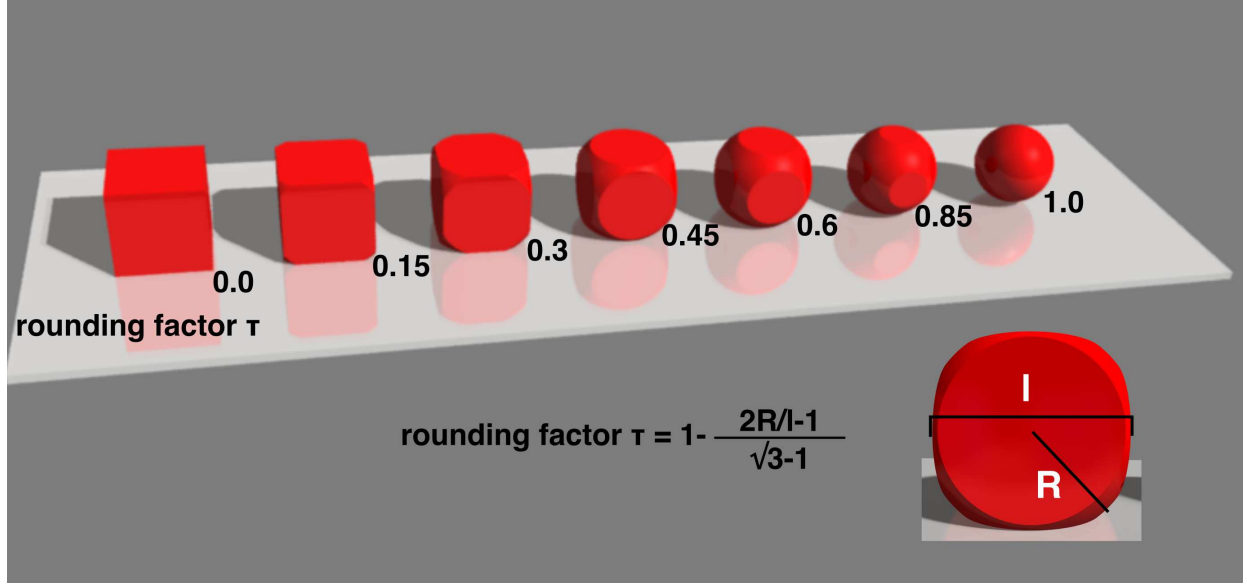


Figure S2: Rounded cube model for the nanoparticle shape: illustration of the shape for different amounts of rounding and definition of the rounding factor  $\tau$  used in modeling.

The model of cubes with a rounded rather than flat truncation is sketched in Fig. S2. It corresponds to the intersection of a cube and a sphere, and as such can also describe perfect cubes and perfect spheres, with rounding parameter  $\tau = 1 - \frac{2R/l-1}{\sqrt{3}-1}$  being 0 and 1, respectively. Intermediate shapes are illustrated in the figure.

The form factor corresponding to this shape is given by the Fourier transform of the shape, as summarized in the following equations:

$$\begin{aligned}
 F_{NP}^{\text{R-Cubes}}(\vec{Q}) &= \mathcal{F}\{\rho_{\text{R-Cubes}}(\vec{r}, l, \tau)\}(\vec{Q}) \\
 \text{with } \rho_{\text{R-Cubes}}(\vec{r}, l, \tau) &= \rho_{\text{Cube}}(\vec{r}, l) \cap \rho_{\text{Sphere}}(\vec{r}, R) \\
 \rho_{\text{Cube}}(\vec{r}, l) &= \begin{cases} \rho_0 & \text{for } |r_x| \leq \frac{l}{2} \wedge |r_y| \leq \frac{l}{2} \wedge |r_z| \leq \frac{l}{2} \\ 0 & \text{else} \end{cases} \\
 \rho_{\text{Sphere}}(\vec{r}, R) &= \begin{cases} \rho_0 & \text{for } |\vec{r}| \leq R \\ 0 & \text{else} \end{cases} \\
 \text{and } \tau_{\text{Round}} &= 1 - \frac{2R/l - 1}{\sqrt{3} - 1} : 0 \leq \tau_{\text{Round}} \leq 1.
 \end{aligned} \tag{1}$$

The Fourier transform here cannot be carried out analytically, and therefore has been calculated numerically on a 3D grid.

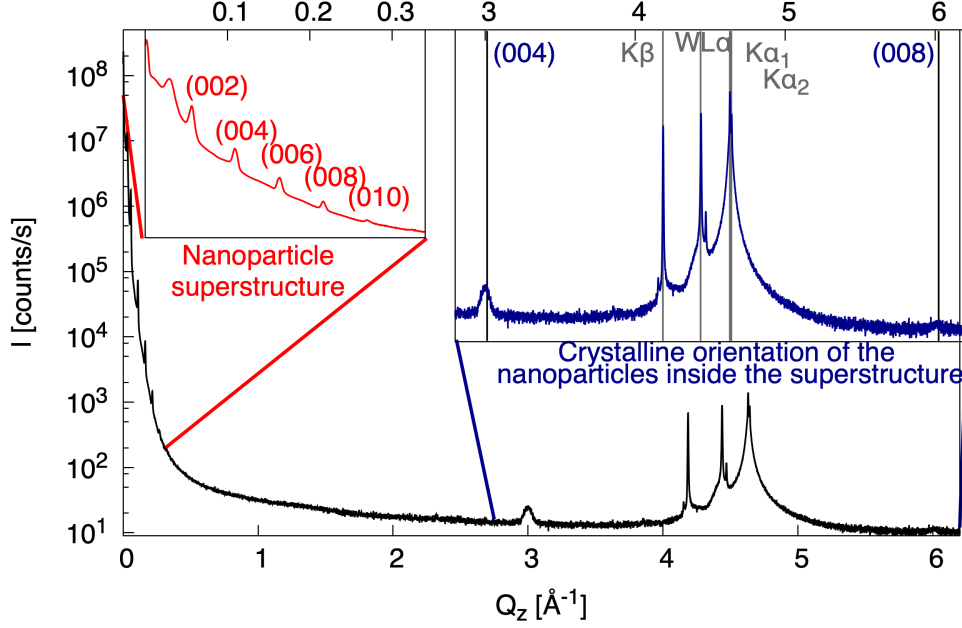


Figure S3: X-ray reflectometry on an ensemble of “nanocube” mesocrystals deposited on a Si(001) substrate. Two insets show magnifications of the curve in two regions. The large sharp peaks indexed in gray are from the substrate, the smaller and broader peaks indexed in blue at small and large  $Q_z$  are from the atomic lattice of the mesocrystals and the row of peaks indexed in red are from the mesocrystal superstructure.

We note that the rounded cube model, like a model with flat truncations, is an idealization. Although the fit to the SAXS data (c.f. Fig. S1) is rather good, deviations from this ideal shape by some of the nanoparticles are likely. In all the modeling done in this paper, we have also assumed that the nanoparticles have a (Log-Normal) size distribution, but the same rounding parameter  $\tau$ , which could not yet be confirmed by experiment as the influence on the radial integrated form factor is very subtle.

## S2. XRR on ensemble of “nanocube” mesocrystals: Orientation of the atomic lattice of individual nanoparticles

The ensemble of mesocrystals of rounded cubic nanoparticles grown on a Si(001) substrate was characterized by x-ray reflectometry (XRR) using a Bruker AXS D8 reflectometer employing Cu  $K\alpha$  radiation. The reflected intensity is shown, in a logarithmic scale, as a function of  $Q_z$  in Fig. S3, with regions containing features further magnified in two insets.

The largest feature consists of a series of sharp peaks resulting from the Si (004) reflection of the substrate. Visible here are the source characteristics, with discrete peaks resulting from Cu  $K\alpha_{1,2}$  and  $K\beta$  as well as W  $L\alpha_{1,2}$  (The tungsten peak occur from the W separation from the cathode and its spread on the anode). The intensity is clearly (note the logarithmic

scale) dominated by the barely resolved Cu  $K\alpha_{1,2}$ , weaker reflections can thus be treated as resulting from Cu  $K\alpha$  radiation.

Clear, though weak and somewhat broad, peaks in the region of  $Q_z$  up to about  $0.3 \text{ \AA}^{-1}$  can be indexed to the mesocrystal superlattice, in agreement with earlier investigations by GISAXS<sup>1</sup> and demonstrating that the  $c$ -direction of the mesocrystals is perpendicular to the substrate. Note that pure (00L) reflections are completely unaffected by the random in-plane orientation of the different mesocrystals of the ensemble.

At higher  $Q_z$ , apart from the substrate peak, two further peaks are visible. These can be indexed as the (004) and (008) reflections of the  $\gamma$ - $\text{Fe}_2\text{O}_3$  (Maghemite) atomic crystal structure ( $Fd\bar{3}m$ , No. 227) of the individual nanoparticles. For randomly oriented atomic crystal structures, many additional peaks should be visible, some of which should have significantly higher intensity. The presence of only these two reflections demonstrates that the atomic lattice  $c$  direction coincides with the mesocrystal  $c$  direction, suggesting a strict orientation of the atomic structure of the rounded nanocubes with regards to the cube faces.

### S3. GISAXS on ensemble of “nanocube” mesocrystals: Lattice constant deviation in an ensemble

The lattice constant distribution over an ensemble of mesocrystals with rounded cubes was determined from the analysis of grazing incidence small angle X-ray scattering (GISAXS) data.

The GISAXS measurement was carried out at the in-house high-brilliance grazing incidence small angle X-ray scattering GISAXS/SAXS instrument GALAXI<sup>2</sup> ( $\lambda = 1.34 \text{ \AA}$ ). The measurement was performed at an incident angle of  $0.4^\circ$ . The structure was fabricated by evaporation-induced self-assembly onto solid substrates (drop casting), which resulted in the formation of ensembles of mesocrystals.<sup>3,4</sup>

The GISAXS data (Fig. S4 left) was processed using the software used and explained in Josten *et al.*<sup>3</sup> It allows the fitting of several peaks with a model incorporating a Gaussian distribution of superlattice tilt angles ( $\sigma_{\text{tilt}_{\text{Ensemble}}}$ ) leading to a tangential peak broadening, lattice constants ( $a$  and  $c$ ) determining peak positions, and a common ( $a$  and  $c$ ) distribution of lattice constants leading to a radial peak broadening ( $\sigma_{\text{lattice}_{\text{Ensemble}}}$ ). Furthermore the in-plane and out-of-plane “GISAXS correlation lengths”  $\epsilon_{ab}$  and  $\epsilon_c$  were determined (note that  $\epsilon$  reflects a combination of the exponential decay of correlations *and* of the finite size of the mesocrystals; these contributions cannot be disentangled for an ensemble of mesocrystals). The fixed peaks were selected based on their optimal signal strength to background ratio. The structural analysis shows that the nanoparticle assemblies display the known<sup>1</sup> body-centered tetragonal structure. The peaks shapes are well described by the used model. Only the peaks along the specular ( $Q_y = 0$ ) line differ from the measurement, as the physics of these are not included in the model, but they are nevertheless sufficiently described for the analysis performed here. Therefore only the peaks along the specular line are weighted by a factor of 10 less compared to the other peaks. The full indexing of the peaks is shown on a sample produced under similar conditions in a previous publication.<sup>4</sup> The chosen peaks are shown in Fig. S4 - Fit. The relevant results are shown in Tab.S1.

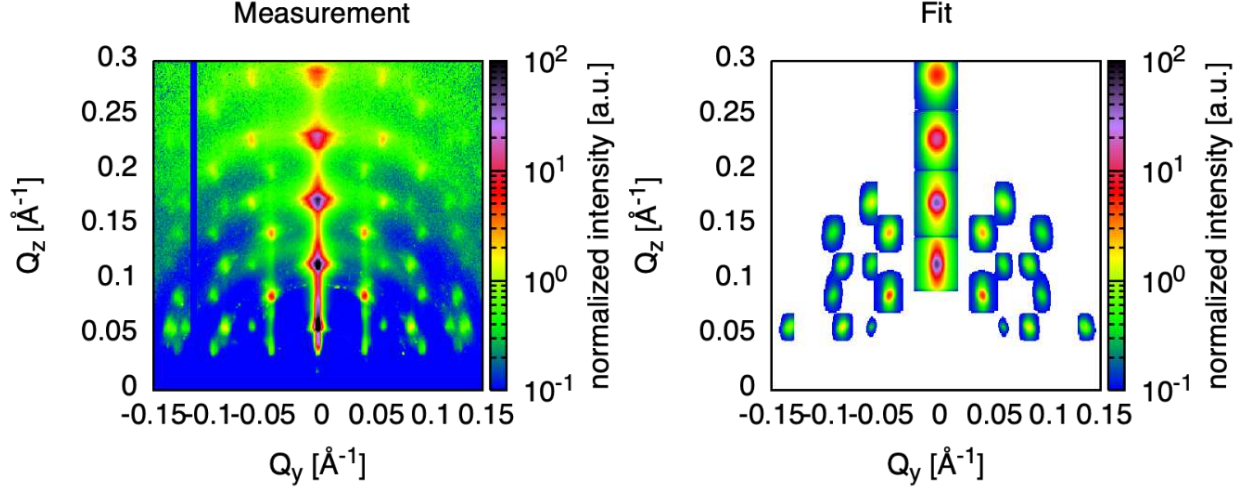


Figure S4: GISAXS measurement of an ensemble of mesocrystals of rounded cube nanoparticles (left) and fit with a model including  $a$  and  $c$  lattice constants, correlation length as well as distributions of lattice constant and tilt angles.

Table S1: Summary of fit results from the GISAXS analysis of an ensemble of mesocrystals of rounded cube nanoparticles.

$a_{Ensemble}$ [nm]	$c_{Ensemble}$ [nm]	$\epsilon_{ab_{Ensemble}}$ [nm]	$\epsilon_{c_{Ensemble}}$ [nm]	$\sigma_{lattice_{Ensemble}}$ [%]	$\sigma_{tilt_{Ensemble}}$ [°]
14.7543(1)	21.575(2)	1145(1)	256.4(2)	2.037(1)	1.0989(4)

These values only come from the bct structure oriented in [001] direction. Very small mesocrystals or mesocrystals with significantly worse crystallinity do not contribute significantly to the Bragg Peaks as observed. The ensemble of mesocrystal observed with GISAXS show an angular spread of about  $1.1^\circ$ , which is a combination of single mesocrystal mosaicity as well as tilting of complete superstructures with respect to the substrate surface normal.

## S4. Sample preparation - mesocrystal extraction

The initial sample from which the individual mesocrystals are extracted, was produced as described in the main text and in<sup>3,4</sup> with optimized parameters to achieve a well ordered structure. Individual single mesocrystals were isolated from the corresponding ensemble of mesocrystals using a focused Ga ion beam (FIB) system in a dual beam FEI Helios NanoLab 400S.<sup>5</sup> This system allows us to cut out the individual crystals with nanometer precision without damaging the crystal structure. A detailed description of the separation process is given and illustrated with some example images in Fig. S5.

First, a mesocrystal which has a certain size and is well separated from others is chosen on the substrate (Fig. S5a). The highly ordered arrangement on top is proved by SEM (Fig.

## Extraction process of a single mesocrystal

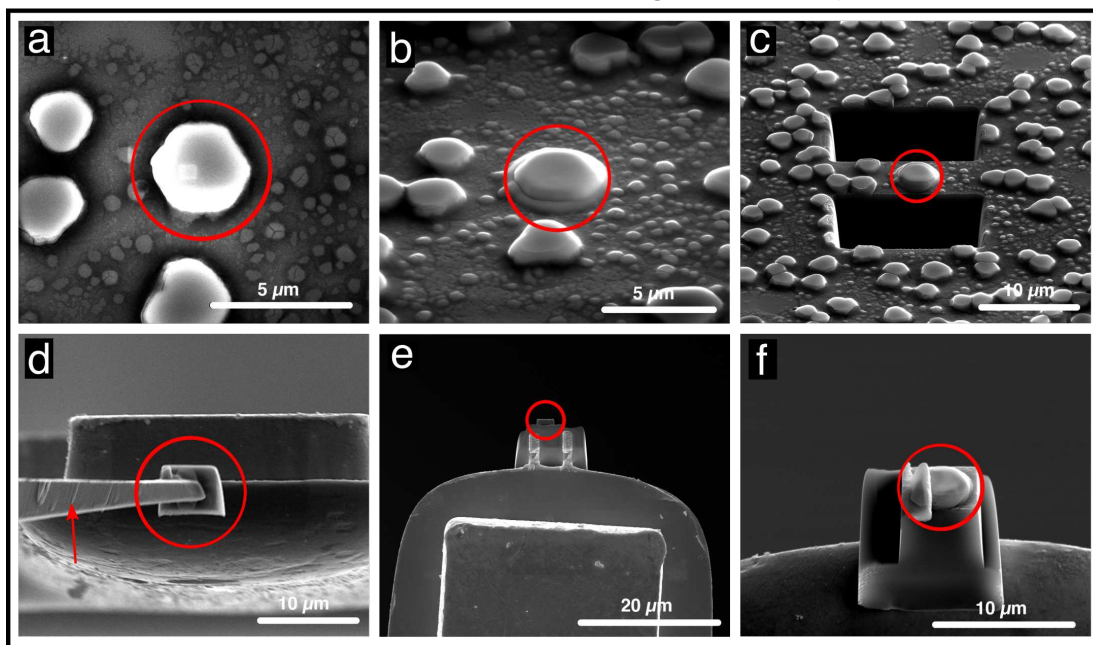
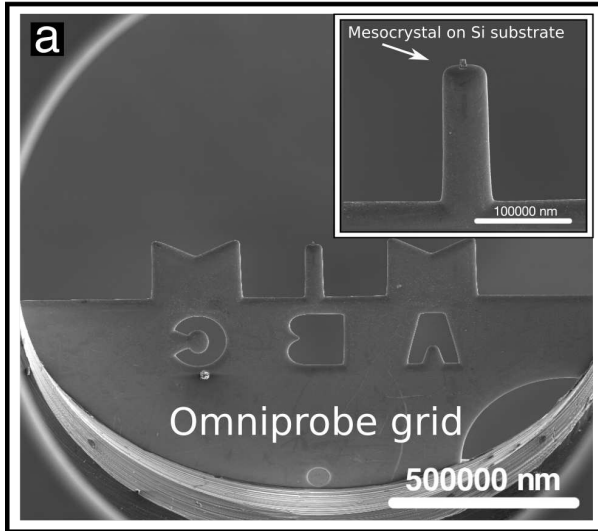


Figure S5: Extraction process of a single mesocrystal, which is described in the text. The position of the mesocrystal is highlighted with a red circle. The red arrow in panel d marks the tungsten manipulator needle.

S6b inset). The mesocrystal was first protected by deposition of a 300 nm thick platinum (Pt) layer using an electron beam of 5 kV and 5.5 nA. Fig. S5b shows a mesocrystal covered with Pt. This layer protects the mesocrystal from the ion beam, which will be used for the extraction process of the chosen mesocrystal. Other mesocrystals around will be destroyed through the extraction process.

For the extraction process, two trenches around the chosen crystal are cut free using an ion beam of 30 kV and 6.5 nA (Fig. S5c). Thereafter, one side block and the bottom area under the sample are also cut free. The block remaining at the end including the sample has to be large enough to allow the fixation with platinum at the tungsten manipulator needle (marked with a red arrow in Fig. S5d). Further on, the last side block is cut free and the mesocrystal is transferred to a standard Cu Omniprobe grid sample holder (Figs. S6a, S5d). The mesocrystal is positioned on top of a finger of the grid, so that a free beam path for the X-rays were possible (Fig. S5e). The orientation of the mesocrystal superstructure is oriented parallel to the grid finger. The block is fixed with platinum (ion beam 30 kV and 93 pA) to the Omnigrid grid (see the stripes of Pt at the backside in Fig. S5e). After loosening the needle, the mesocrystal is cut freely on the sides and cleaned using a low ion beam of 30 kV and 93 pA. During this process, images are taken continuously and Fig. S5f shows an intermediate step in the free cutting process. The resulting isolated single mesocrystals were then ready for structural characterization in a defined orientation and geometry (Fig. S6b).

## Mounted mesocrystal on sample holder



## Cubic Nanoparticles

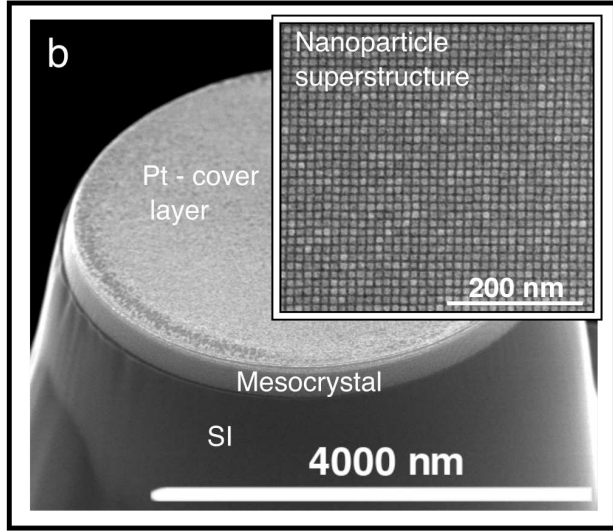


Figure S6: (a) SEM picture of a part of the Cu Omniprobe grid, which is a typical TEM lift-out grid. The inset displays a zoom of the central pin on which a free-cut part of the silicon substrate with a mesocrystal on top is attached. (b) SEM picture of the investigated single mesocrystal of cubic nanoparticles grown on a Si substrate, with a Pt cover layer, after being cut free with a focused ion beam. The inset shows the regular cubic arrangement of the nanoparticles taken before the Pt deposition

## S5. Single meso-crystal diffraction: Alignment procedures, mapping of reciprocal space planes and rocking curves

### S5.1 Alignment

The alignment of the mesocrystal has to take into account both rotation (the orientation of the mesocrystal) and translation (having the small mesocrystal centered in the focused beam), which was facilitated by mounting the omniprobe grid (c.f. Fig. S6a), containing the mesocrystals, on a small goniometer. The alignment started by locating the approximate position of the cut Si substrate optically, making use of the Cu omniprobe grid. The top of the Cu pin containing the sample was then pinpointed by measuring the beam attenuation using a NaJ point detector. We then switched to a Roper Scientific area detector and located the (004) reflection of the Si substrate ( $2\theta \sim 43^\circ$ ), scanning  $\omega$  and translations.

The Si (004) reflection was then used to adjust the goniometer angles and translations such that the Si [001] direction (which also corresponds to the mesocrystal [001] direction) coincided with the  $\varphi$ -axis (see Fig. 2a for the definitions of the diffractometer angles) and the substrate was in the center of rotation of the diffractometer. The detector was then driven to zero angle, with the detector area covering angles up to about  $3^\circ$ , a beamstop added, and the reflections of the mesocrystal were located, first the (00L) reflections that are independent of  $\varphi$ , then additional reflections. The goniometer settings were then fine-tuned in order to

maximize the intensities of the mesocrystal reflections.

The beam focus ( $5\ \mu\text{m} \times 10\ \mu\text{m}$ ) was smaller than the sphere of confusion of the diffractometer, i.e. the spread of the center of rotation of different diffractometer axes, which in this case has a diameter of about  $15\ \mu\text{m}$ .<sup>6</sup> Therefore, after large changes of  $\varphi$  and particularly  $\chi$ , the mesocrystal ( $0.196\ \mu\text{m} \times 4.5\ \mu\text{m}$ ) needed to be recentered in the beam, which was done by translations of the diffractometer table, maximizing reflection intensities.

## S5.2 Mapping of reciprocal space planes

With the mesocrystal aligned as described in Sec. S5.1, all reciprocal space planes containing reflections can be selected by a simple  $\varphi$  rotation. For the large unit cell of the mesocrystals and the wavelength of  $1\ \text{\AA}$ , the Ewald sphere is rather flat (similar as with e.g. 100 keV x-rays and typical atomic (small molecule) crystals), implying that often many reflections of the selected reciprocal space plane are excited. Nevertheless, the reflections are not all in optimal reflection condition, and to get the contribution of all the reflections of the plane that are in range, it is necessary to rock the crystal both vertically (in  $\omega$ ) and horizontally (in  $\varphi$ ) around the optimal position (indicated by similar intensities left and right, and top and bottom), adding the obtained intensities. This corresponds approximately to an integration in  $Q_x$  direction, though with a wider range further away from the origin (see Fig. 2a for the definitions of the reciprocal space coordinate system for one plane as well as for the angles).

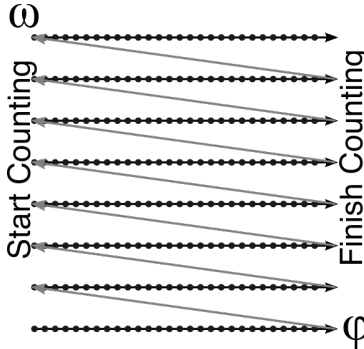


Figure S7: Sketch of the used meshes in  $\varphi$  and  $\omega$ .

This was done by driving meshes as sketched in Fig. S7.  $\omega$  was set in five discrete steps, spanning a range of  $\pm 1^\circ$  around the optimal position. For each  $\omega$  position,  $\varphi$  was scanned in the range of  $\pm 3.5^\circ$  with 70 steps taking 1 minute, during which the detector was continuously exposed. The resulting five detector images, already naturally integrated in  $\varphi$ , were then added together, providing integration in  $\omega$ .

All received reciprocal space maps, for a mesocrystal of cubic nanoparticles, are shown in Fig. S8, except the (h0l) plane which is shown in Fig. 2 of the paper. The reciprocal space maps were used for the determination of reflection widths and the analysis of the various contributions to the broadening of reflections (see Sec. S6). However, this procedure is not optimally suited to obtain reliable intensities. Intensities used for the structural refinement were instead collected by  $\omega$  rocking scans as detailed below.

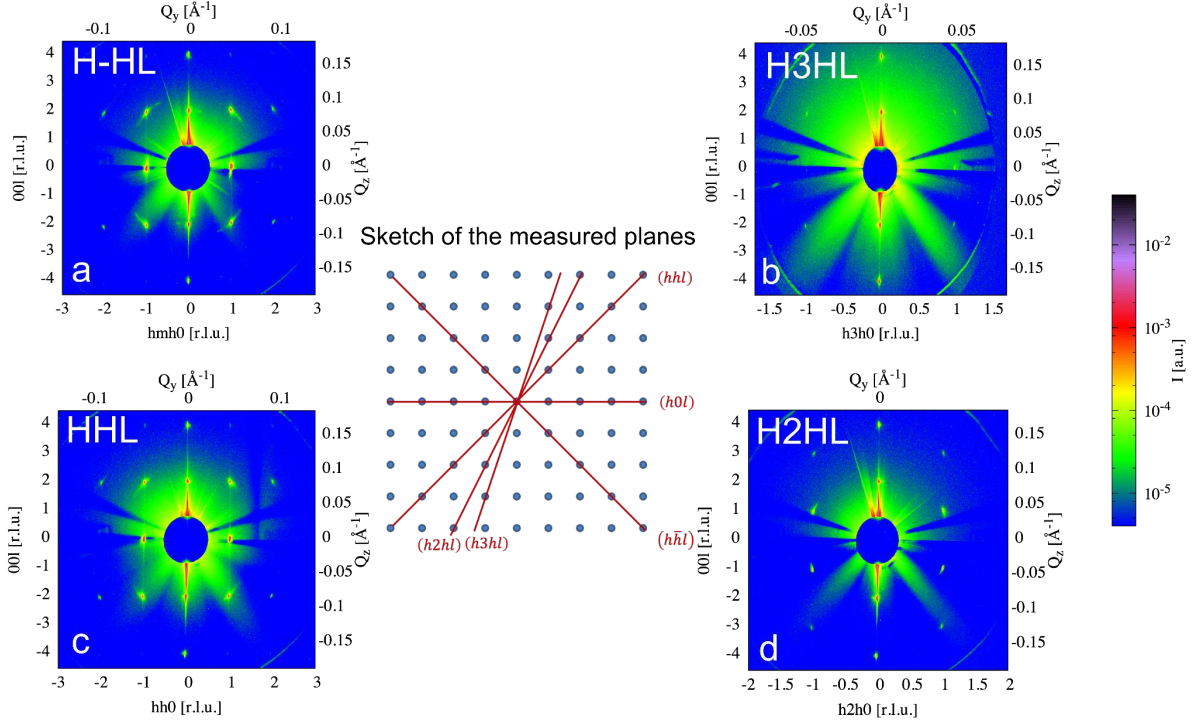


Figure S8: Scattering patterns of all reciprocal lattice planes with indexed Bragg reflections to determine the crystal structure, apart from the  $(h0l)$  plane which is shown in Fig. 2b: a)  $(h-hl)$  plane b)  $(h3h0)$  plane c)  $(hh0)$  plane d)  $(h2h0)$  plane

### S5.3 Rocking curves and integrated intensities

In order to obtain 3D integrated intensities for structural refinement, rocking scans were performed. First, all reciprocal space planes reachable by rotating  $\varphi$  (see Fig. 2a for the angle definitions) were subsequently selected. Then, for each reflection in that plane, the reflection was brought into vertical position by adjusting the  $\chi$  angle if necessary (i.e. for non- $00L$  reflections). Despite of the high precision of the diffractometer, after each change of  $\chi$  the sample table has to be shifted in  $y$  and  $z$  directions to optimize the sample illumination, the main source of the relatively large spread of intensities of different observations of equivalent reflections (see Fig. S10b). Detector images were then taken as a function of  $\omega$  over a region of  $\sim \pm 3^\circ$ .

For each  $\omega$  position and reflection two rectangular regions around the reflection are defined as shown in Fig. S9. The outer region (excluding the inner region) is used to estimate the background contribution. A 2d parabola function is fit to the background region and then subtracted from the data. The inner rectangle is then summed up to get the intensity.

This results in rocking curves of detector-integrated intensity vs  $\omega$ , a few examples of which are shown in Fig. S10. The rocking curves are then integrated numerical using the trapezoidal rule to give the overall integrated intensity of one peak. As the proper integrated intensity is defined in terms of integration in reciprocal space (rather than detector and rocking angle), the obtained intensity is then corrected by a Lorentz-factor

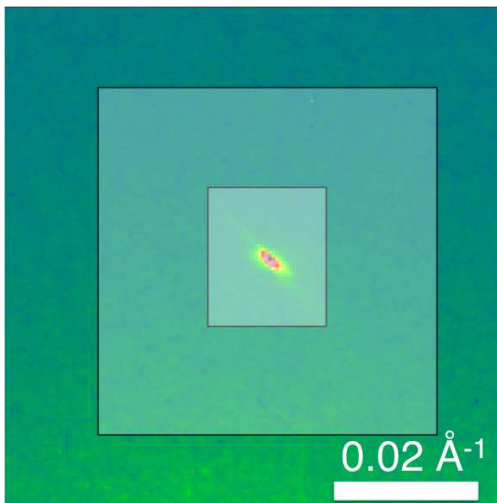


Figure S9: Definition of the regions for the integration and background determination for reflections on the detector.

$L \propto 1/(\sin \theta \cos \theta) \sim 1/\sin \theta$ . Note that no polarization factor correction is necessary because  $\cos 2\theta \sim 1$  for the small scattering angles used here.

Given that we have planes aligned prior to rocking, a single rocking scan will give detector-integrated intensity vs  $\omega$  curves for several reflections, including reflections that are not aligned vertically. The latter reflections can be used as well, with the appropriately modified Lorentz-factor  $1/(\sin \theta \cos \psi)$ , where  $\psi$  is the angle between the reflection and the vertical direction. Overall, the procedure leads to many observations of the same reflections with different azimuths: we used 74 observations (see table S2) for 9 reachable (moving the detector would in principle allow to reach more reflections, but the intensity falls very quickly with  $Q$ , making their collection not feasible) unique reflections, corresponding to a redundancy of 8.2. The internal  $R$  value<sup>7</sup>

$$R_{\text{int}} = \frac{\sum_{HKL} \sum_i |I_i(HKL) - \overline{I(HKL)}|}{\sum_{HKL} \sum_i |I_i(HKL)|} = 0.26 \quad (2)$$

is quite high compared to typical x-ray diffraction datasets from small-molecule crystallography, which we attribute to the small size of sample and beam focus relative to the diffractometer sphere of confusion (c.f. Sec. S5.1).

One potential reason for large  $R_{\text{int}}$  values is absorption. In our case, however, the smallness of the sample renders any absorption correction very small. Taking into account the Maghemite crystal structure and density of the nanoparticles and their volume fraction of about 63%, we obtain an attenuation length of about  $49 \mu\text{m}$ , which for the direct beam going through the middle of the sample leads to an attenuation of just 9.6% (through the Si pin below the sample the attenuation is even less, about 3%). Furthermore, given the small scattering angles of below  $3^\circ$ , the contributing beam paths through the sample will be rather similar, which should lead to variations between different observations associated with absorption that are far below 1%. As can be seen in table S2 and in Fig. S10b, experi-

Table S2: Integrated intensities of the reflexes used from mesocrystal with rounded cubic particles.

plane	(hkl)	$\chi$ [°]	$I_L$ [a.u.]	(hkl)	$\chi$ [°]	$I_L$ [a.u.]		
<b>(h0l)</b>	(002)	0	3.487474	(00-2)	0	4.417417		
		38	1.164279		38	0.641937		
		38	3.622978		38	2.885802		
	(004)	0	1.005613	(00-4)	0	1.556463		
		(10-1)	49		15.478618	(101)	49	10.009986
			90		25.605288		7	20.418253
	(-10-1)	83	25.703287	(-101)	0	24.252295		
		49	8.949295		7	18.577848		
		90	13.846430		0	21.747679		
	(200)	83	22.967346	(-200)	49	13.498137		
		90	6.980267		90	4.685243		
		48	2.934401		48	0.260197		
	(-202)	48	7.982461	(20-2)	48	6.563991		
		49	0.041254		49	0.137136		
		(202)	49		0.030219	(-20-2)	49	-0.242451
<b>(hhl)</b>	(002)	0	3.218481	(00-2)	0	2.946105		
		52	2.442972		52	1.214388		
		52	2.142512		52	3.271747		
	(004)	0	1.494645	(00-4)	0	1.068915		
		(110)	90		18.675230	(-1-10)	90	17.953444
			37		12.848164		37	11.278361
	(112)	37	13.273435	(-1-1-2)	37	11.700269		
		39	4.309290		39	2.814963		
		0	4.480233		77	4.639545		
	(11-2)	13	4.176178	(-1-12)	90	3.868875		
		39	4.221046		39	4.980977		
		77	4.403585		0	6.058261		
	(220)	90	4.684094	(-2-20)	13	3.492749		
		90	1.194695		90	-0.261204		
		(002)	0		4.353100	(00-2)	0	5.291287
70	1.936964		70	1.402490				
70	1.399625		70	2.002487				
(004)	0	1.485221	(00-4)	0	1.112317			
	(121)	68		1.869076	(-1-2-1)	68	1.481820	
		0		3.255261		43	3.034235	
(12-1)	68	2.721400	(-1-21)	68	2.503764			
	43	3.043836		0	2.937242			

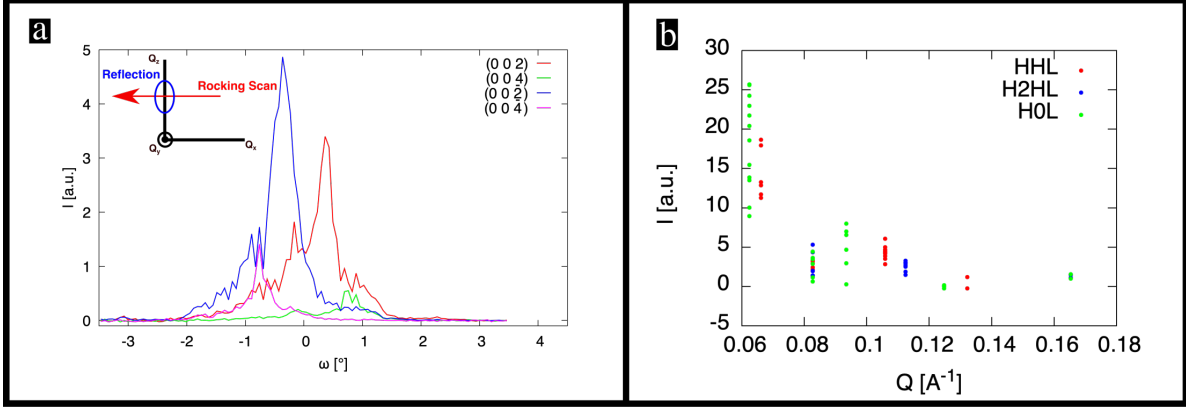


Figure S10: Rocking scans and integrated intensities on the mesocrystal of rounded nanocubes. (a) Rocking curves (measured data thick lines) for various (00L) reflections, obtained by scanning  $\omega$  with the sample aligned as for the measurement in Fig. 2a. Under these conditions, the rocking scan corresponds to a scan through the reflection along  $b^*$ , as sketched as inset. (b) Integrated intensities for different reflections in to show the large spread of the intensities.

mentally observed variations are much higher than 10%. Absorption issues therefore have a very minor, if not negligible, impact on the data set, and consequently we did not carry out an absorption correction.

## S6. Single meso-crystal diffraction: Analysis of Bragg-peak shapes from reciprocal space planes

To extract structural information about the mesocrystals consisting of cubic particles we have analyzed the peak shapes by extracting horizontal and vertical peak widths from the images of all measured scattering planes. In addition to the experimental resolution, the peak widths are determined by crystal structure parameters, namely the correlation lengths, finite size effects, lattice constant distributions and mosaicity. The individual contributions are sketched in Fig. S11.

### S6.1 Extraction of peak widths

To extract the two standard deviation parameters for each Bragg-peak a 2D Gaussian profile [Eqn. (3)] was fitted to the dataset using the Levenberg-Marquard algorithm. The refined parameters were the peak positions ( $Q_{y0}/Q_{z0}$ ), standard deviations ( $\sigma_{Q_y}/\sigma_{Q_z}$ ), scaling ( $A$ ) and background ( $C$ ).

$$I(Q_y, Q_z) = A \cdot e^{-\frac{1}{2} \left( \frac{(Q_y - Q_{y0})^2}{\sigma_{Q_y}^2} + \frac{(Q_z - Q_{z0})^2}{\sigma_{Q_z}^2} \right)} + C \quad (3)$$

The refinement area was a quadratic region of  $\pm 3 \cdot 10^{-3} \text{\AA}^{-1}$  in  $Q_y$  and  $Q_z$  around the peak position.

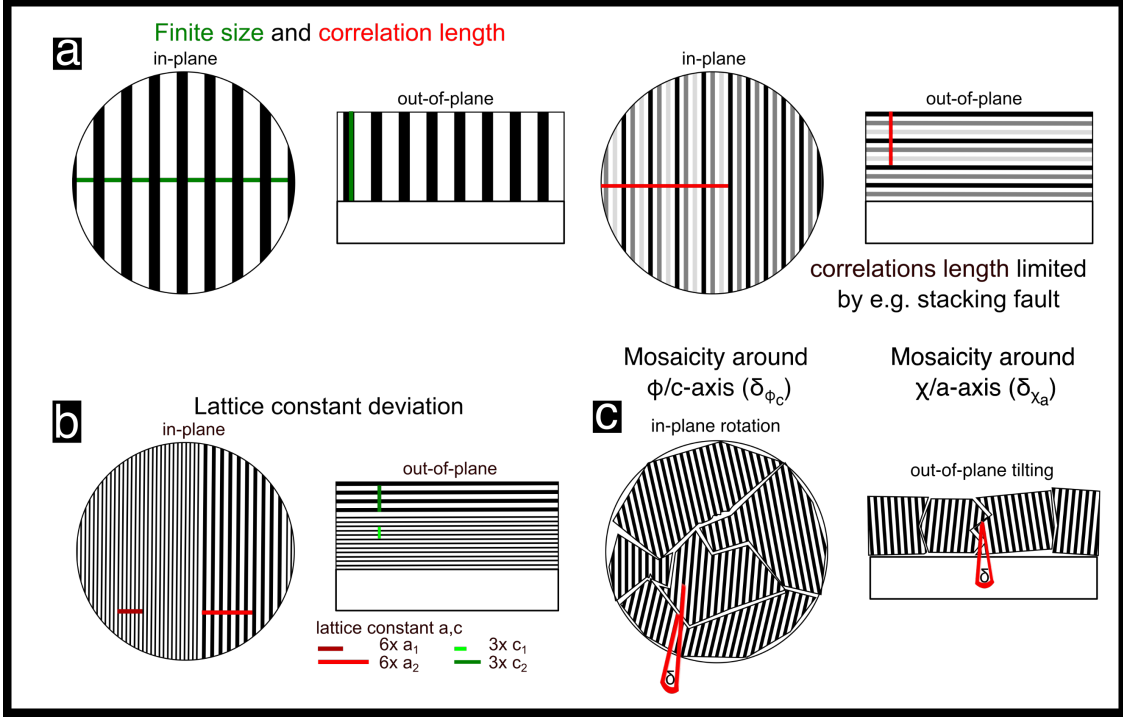


Figure S11: Schematic illustration of different sources of reflection broadening. (a) Finite sample size and correlation length, in- and out-of-plane. (b) Strain, i.e. distribution of  $a$  and  $c$  lattice constants. (c) Mosaicity (distributions of tilts), i.e. rotation of different crystallites around  $\varphi$  or  $\chi$  axes.

## S6.2 Refinement of components to standard deviations

The different components that contribute to the peak shape contribute differently for each reflection in dependence of its  $Q_y$  and  $Q_z$  position.

**Tilt distribution/mosaicity** Only the mosaicity around the  $Q_x$  direction contributes to the peak shape on the 2D detector. This contribution is a broadening around the tangential direction with a fixed angular size, therefore it scales with the length of the  $(Q_y, Q_z)$  vector. The components of this broadening are the projections of this tangential broadening onto the  $Q_y$  or  $Q_z$  axis. It follows that:  $\sigma_{m|y} = \sigma_m \cos \chi = C_m Q_z$  and  $\sigma_{m|z} = \sigma_m \sin \chi_a = C_m Q_y$  where the scaling constant can be described in terms of mosaic angular spread as  $C_m = \tan \sigma \chi_a$ . In the further course of the manuscript,  $\sigma \chi_a$  is referred to as  $\sigma_{tilt}$ .

**Correlation/finite size** Crystallite domain size or finite size is the limitation of the coherent scattering volume in a given direction. This is a general property of the crystal system that equally effects each Bragg-peak and is thus a constant component for the peak shape uniform for all reflections ( $\sigma_y$  and  $\sigma_z$  as used later on include also uniform instrumental contributions).

**Lattice parameter distribution** If different crystal domains show a variation in lattice parameter their peak positions will shift by the same fraction, thus leading to a peak

broadening that scales with that reciprocal space component for the reflection:  $\sigma_{\sigma a|y} = \sigma a \cdot Q_y$  and  $\sigma_{\sigma c|z} = \sigma c \cdot Q_z$ . For the analysis used, the values for both directions ( $\sigma a$  and  $\sigma c$ ) were coupled and designated as  $\sigma_{lattice}$ .

**Instrumental resolution** The measurement resolution is also a constant contribution that is given by the beam divergence and distance of the detector as well as intrinsic detector resolution (The resolution based on the energy uncertainty is negligible). For the different directions we estimate the following values: resolution (FWHM) in y (or rather a, in-plane) direction is  $1.5(3) \cdot 10^{-3} \text{ \AA}^{-1}$  and the resolution for the out-of-plane direction (z or c-direction) is  $0.5(1) \cdot 10^{-3} \text{ \AA}^{-1}$ .

The measured peak is a convolution of all of these effects. Assuming for simplicity a Gaussian shape function for each component the resulting peak shape should again be a Gaussian with a variance that is the sum of all contributing variances. We can therefore describe the two standard deviations extracted from each peak as:

$$\sigma_{Q_y} = \sqrt{\sigma_y^2 + \sigma_{\sigma a|y}^2 + \sigma_{m|y}^2} = \sqrt{\sigma_y^2 + (Q_y \cdot \sigma a)^2 + (Q_z \cdot \tan \sigma \chi_a)^2} \quad (4)$$

$$\sigma_{Q_z} = \sqrt{\sigma_z^2 + \sigma_{\sigma c|z}^2 + \sigma_{m|z}^2} = \sqrt{\sigma_z^2 + (Q_z \cdot \sigma c)^2 + (Q_y \cdot \tan \sigma \chi_a)^2} \quad (5)$$

### S6.3 Error estimation

We have found a considerable spread in the standard variation values when comparing the values of symmetry equivalent reflections. This is likely due to the structured background from various scattering effects that influence the fits. For this reason the errors on the fit parameters cannot be extracted from the individual peak refinements directly.

To still get a sensible estimate of the refinement of the structural parameters from equations (4) and (5) we have assumed that the horizontal and vertical components in one scattering plane have equal errors, a correct refinement should yield a  $\chi^2/DOF = 1$  and performed the refinement to the standard deviation as follows:

1. Refine equations (4) and (5) to the extracted standard deviations without error bars.
2. Use the refined parameters to calculate  $\chi^2$  values for the horizontal and vertical components and define the errors as  $\sigma_0 \sigma_{Q_y/Q_z} = \sqrt{\frac{2\chi_{y/z}^2}{DOF}}$  to get a good estimate of the relative error of the two directions.
3. Repeat refinement with error bars, due to the different weighting small changes (a few %) of the resulting parameters were found.
4. Re-normalize the error bars to the new refinement as  $\sigma \sigma_{Q_y/Q_z} = \sigma_0 \sigma_{Q_y/Q_z} \sqrt{\chi^2/DOF}$
5. Repeat refinement with new error bars (same results but yielding  $\chi^2/DOF = 1$ ) and extract the parameter errors from that refinement.

With this procedure we could extract the structural parameters for the mesocrystal for each individual scattering plane that was measured. The peak standard deviations with their errors were then combined from all scattering planes to refine an average set of structure parameters that is reported in the main article.

## S6.4 Fit results

An example of the parameter refinement for all peaks is shown in Fig. S12 with individual Bragg-peak results indexed according to the absolute value of H/L ( $Q_y$ ) or L/H ( $Q_z$ ). The indicated error-bars are the estimated values according to section S6.3.

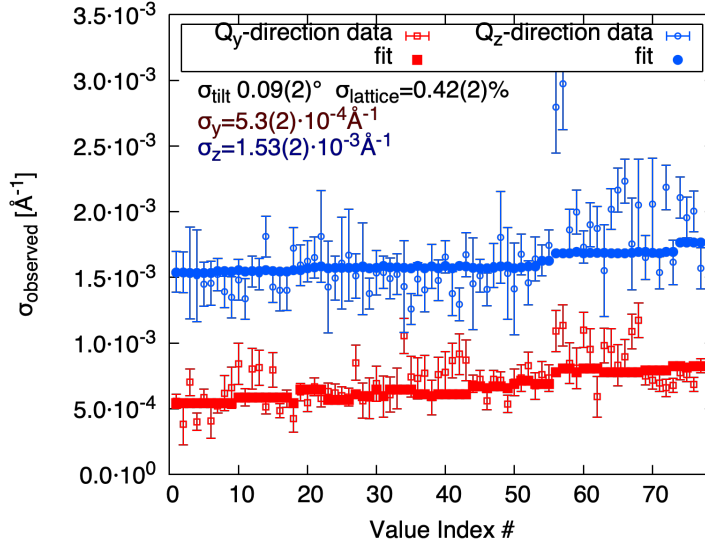


Figure S12: Fit results to the complete set of scattering plane peak standard deviations

The fit parameters comprise of in- and out-of-plane uniform parts (Correlation/finite size, but also including instrumental broadening/resolution), lattice parameter distribution, and tilt distribution, as detailed in Sec. S6.2 above. The obtained values are summarized in the table below:

Table S3: Summary of fit results from the peak shape analysis.

$\sigma_{y_{Meso}}$ [ $\text{\AA}^{-1}$ ]	$\sigma_{z_{Meso}}$ [ $\text{\AA}^{-1}$ ]	$\sigma_{lattice_{Meso}}$ [%]	$\sigma_{tilt_{Meso}}$ [°]
$5.3(2) \cdot 10^{-4}$	$1.53(2) \cdot 10^{-3}$	0.42(2)	0.09(2)

## S6.5 Constant parts of the broadening: finite size and correlations

For the uniform parts of the broadening ( $\sigma_y$  and  $\sigma_z$  in table S3), there can be three distinct contributions (c.f. Sec. S6.2): i) instrumental, ii) finite-size effects, and iii) finite correlation length. The last, assuming exponentially decaying correlations, leads to a Lorentzian peak-shape and the sample finite size leads to a broadening described by the Laue-function with a shape that is closer to Lorentzian than to Gaussian, while the shape of the instrumental contribution may be close to rectangular. The overall uniform part of the broadening is the convolution of these three contributions. Although the fit done in Sec. S6.4 assumed Gaussian line-shapes, for trying to disentangle the different contributions i) to iii) here, we remove this assumption, and instead of the standard deviations consider the full-widths at half maximum (FWHM), which is given by  $FWHM_{exp,a/c} = 2\sqrt{2\ln 2} \cdot \sigma_{y/z}$ . The in-plane

overall uniform broadening  $FWHM_{exp,a} = 1.25(5) \cdot 10^{-3} \text{ \AA}^{-1}$  is already fully accounted for by the instrumental contribution  $FWHM_{i,a} = 1.5(3) \cdot 10^{-3} \text{ \AA}^{-1}$  and thus neither finite-size effects nor effects from finite correlations are discernible.

This is not the case for out-of-plane, where the instrumental contribution  $FWHM_{i,c} = 0.5(1) \cdot 10^{-3} \text{ \AA}^{-1}$  is much smaller than the overall uniform broadening  $FWHM_{exp,c} = 3.60(5) \cdot 10^{-3} \text{ \AA}^{-1}$ . Deconvolution of the instrumental contribution depends on its line-shape (FWHM of two Lorentzians add linearly, whereas the FWHM of a Lorentzian and a rectangular function add quadratically). Considering shapes in between those extremes and the error bars, the deconvoluted  $FWHM_{ii+iii,c}$  should be in the range of  $\sim 2.95 - 3.63 \cdot 10^{-3} \text{ \AA}^{-1}$  (with a Lorentzian shape).

From SEM and according to the spacing of the Laue oscillations ( $N_L = 13$ ) and lattice parameter  $c$ , the thickness of the mesocrystal is  $D_c = 196(1) \text{ nm}$ . The corresponding FWHM of the Laue function is

$$FWHM_{ii,c} = \frac{0.89 \cdot 2\pi}{D_c} = 2.85(2) \cdot 10^{-3} \text{ \AA}^{-1}. \quad (6)$$

This is certainly the dominant contribution to  $FWHM_{exp,c}$ , not unexpected given the clear observation of the Laue oscillations in Fig. 2b. A possible contribution of finite correlations broadening  $FWHM_{iii,c} \sim 0.08 - 0.8 \cdot 10^{-3} \text{ \AA}^{-1}$  remains, which would correspond to a correlation length in the range  $\xi_c \sim 0.25 - 2.5 \text{ \mu m}$ . However, the approximation made in fitting the overall widths as Gaussians leads to additional uncertainty that disproportionately affects a small rest-contribution such as  $FWHM_{iii,c}$  here. Therefore, we refrain from stating a range for  $\xi_c$  in the main text. Clear is, however, that the  $c$  correlation length is much larger than the sample thickness.

## S7. Single meso-crystal diffraction: Structural analysis

The 9 corrected and merged integrated intensities (see Sec. S6.3) were modeled using an isotropic Debye-Waller factor and the structure factor of the mesocrystal unit cell, consisting of two particles with their edges aligned (see main text) to the unit cell axes. The body-centered structure implies the reflection condition  $H + K + L$  even, which was fulfilled for all experimentally observed reflections. The *anisotropic* form factor used for the particles was the Fourier transform of a rounded cube, as described in Sec. S1.2. The size distribution of the nanoparticles was taken into account by convolution with a lognormal distribution. This modeling corresponds to the ‘‘local monodisperse approximation’’ used in SAXS analysis<sup>8</sup> and neglects effects on the interference. This is reasonable, since a local size variation would merely lead to diffuse scattering and a corresponding decrease of the intensity of the Bragg peaks analogous to the effects of random displacements. Thus any such effect is included by fitting a Debye-Waller factor. Including a common scale factor  $I_0$ , the overall model can be described as

$$I_{HKL} = I_0 \cdot \int_{-\infty}^{\infty} \frac{1}{l'} e^{-\frac{(\ln l' - \ln(l' \sqrt{1 + \sigma_l^2/l^2}))^2}{2 \ln(1 + \sigma_l^2/l^2)}} \mathcal{F} \{ \rho_{R-Cubes}(\vec{r}, l', \tau) \} \left( \vec{Q}_{HKL} \right) dl' \cdot e^{-\frac{1}{3} a_{DW}^2 \cdot Q_{HKL}^2}, \quad (7)$$

for  $H + K + L$  even and contains 5 fit parameters. Refinements of the intensities was done using a standard error-weighted least-squares refinement with the mpfit implementation of the Levenberg-Marquard algorithm. For the rounded cubes form factor a numeric integration of the particle density was used. Different integration grid sizes ( $25^3, 50^3, 100^3$ ) were calculated which all yielded indistinguishable fit results and intensities.

Table S4: Comparison of the merged measured intensities of unique mesocrystal reflections and the calculated intensities of the optimized model.

Reflection	Measured Intensity	Modelled Intensity
(1 0 1)	$1.843(569) \cdot 10^5$	$1.989 \cdot 10^5$
(1 1 0)	$1.429(293) \cdot 10^5$	$1.018 \cdot 10^5$
(0 0 2)	$2.658(1251) \cdot 10^4$	$3.884 \cdot 10^4$
(2 0 0)	$4.901(2647) \cdot 10^4$	$9.605 \cdot 10^4$
(1 1 2)	$4.344(758) \cdot 10^4$	$1.911 \cdot 10^4$
(1 2 1)	$2.606(585) \cdot 10^4$	$1.647 \cdot 10^4$
(2 0 2)	$-0.085(1413) \cdot 10^3$	$4.217 \cdot 10^3$
(2 2 0)	$4.667(7279) \cdot 10^3$	$0.375 \cdot 10^3$
(0 0 4)	$1.287(228) \cdot 10^4$	$1.206 \cdot 10^4$

Given the relatively small observations to parameter ratio, the cube rounding parameter  $\tau$  was fixed at several values. We have found that  $\chi^2$  did not increase much for  $\tau$  in the range 0.7–0.9 and that most of the fitted parameters did not change significantly either: a clear correlation with  $\tau$  was found only for the Debye-Waller factor  $a_{DW}$ . The final fit was performed with  $\tau$  fixed to 0.8, the value obtained from SAXS (see Sec. S1). Table S4 lists the observed and calculated intensities, with the errors in the observed intensities obtained from the standard deviation of the different observations of each of the symmetry-unique reflections (c.f. table S2). The corresponding reduced  $\chi^2$  value of 5.8 is relatively high, suggesting that the model may be too simple (e.g. the assumption of no variation of  $\tau$ ) to fully describe the data. From the table we can also determine for comparison the standard crystallographic  $R$ -values:<sup>7</sup>  $R_1 = \sum ||F_o| - |F_c|| / \sum |F_o| = 0.23$ ,  $wR_2 = \sqrt{\sum w(I_o - I_c)^2} / \sum wI_o^2 = 0.47$ . These residuals are in the range of typical  $R$  values observed for complex macromolecules and much higher than usual for small molecules. However, they have to be expected given the also high  $R_{\text{int}} = 0.26$  (c.f. Sec. S6.3) and the relatively simple model used, which e.g. doesn't allow for any shape-variations between the different nanoparticles of the mesocrystal.

The optimal model parameters are listed in table 1 in the main text. The refinement errors for the resulting parameters were non-trust worthy (e.g. error on the size distribution far bigger than 100% size variation), which we attribute to the numerical form factor that was used. Instead we used a manual estimation of errors which lead to a larger than 5% increase in  $\chi^2$ . These estimated errors compared well to the fit error for intensity and edge length if only these two parameters where refined, parameters that did not change the numerical integration and thus behaved normally.

The small value of the average displacement suggests that the nanoparticle positions are well fixed by their neighbors, as may be expected (Fig. 2d). The particle size distribution of 0.0(26)% is unfortunately limited in quality by the data but is consistent with the distribution

of lattice parameters ( $\sigma_{a_{Meso}}$  and  $\sigma_{c_{Meso}}$  in table S3), which is as expected: larger particles lead to larger lattice constants.

## References

- (1) Disch, S.; Wetterskog, E.; Hermann, R. P.; Salazar-Alvarez, G.; Busch, P.; Brückel, T.; Bergström, L.; Kamali, S. *Nano Lett.* **2011**, *11*, 1651–1656.
- (2) Jülich Centre for Neutron Science (2016). GALAXI: Gallium anode low-angle x-ray instrument. *Journal of large-scale research facilities* *2*, A61. <http://dx.doi.org/10.17815/jlsrf-2-109>.
- (3) Josten, E.; Wetterskog, E.; Glavic, A.; Boesecke, P.; Feoktystov, A.; Brauweiler-Reuters, E.; Rücker, U.; Salazar-Alvarez, G.; Brückel, T.; Bergström, L. *Scientific Reports* **2017**, *7*, 2802.
- (4) Wetterskog, E.; Klapper, A.; Disch, S.; Josten, E.; Hermann, R. P.; Rücker, U.; Brückel, T.; Bergström, L.; Salazar-Alvarez, G. *Nanoscale* **2016**, *8*, 15571–15580.
- (5) Kruth, M.; Meertens, D.; Tillmann, K. *Journal of large-scale research facilities JLSRF* **2016**, *2*.
- (6) Seeck, O. H.; Deiter, C.; Pflaum, K.; Bertam, F.; Beerlink, A.; Franz, H.; Horbach, J.; Schulte-Schrepping, H.; Murphy, B. M.; Greve, M.; Magnussen, O. *Journal of Synchrotron Radiation* **2012**, *19*, 30–38.
- (7) Ladd, M.; Palmer, R. *Structure Determination by X-ray Crystallography*; Springer, 2014.
- (8) Pedersen, J. S. *Journal of Applied Crystallography* **1994**, *27*, 595–608.